Materials Advances

ROYAL SOCIETY OF CHEMISTRY

PAPER

View Article Online
View Journal

Check for updates

Cite this: DOI: 10.1039/d6ma00275g

Influence of pressure-induced structural change in Al_2O_3–SiO_2 glasses on the sound velocity and Poisson's ratio under pressure

Itaru Ohira, *[a] Yoshio Kono, [b] Steeve Gréaux, [c] Sayako Inoué, [c] Nozomi M. Kondo, [d] Sho Kakizawa, [e] Yuji Higo, [e] Noriyoshi Tsujino, [e] Rostislav Hrubiak, [f] Guoyin Shen [f] and Atsunobu Masuno [g]

Received 27th February 2026,
Accepted 22nd April 2026

DOI: 10.1039/d6ma00275g

rsc.li/materials-advances

In this study, we investigated pressure-induced changes in the structure and elastic properties of $x\mathrm{Al_2O_3}$–$(100 - x)\mathrm{SiO_2}$ glasses (x = 29, 36, 43, 50, 60 mol%; referred to as xAS) by *in situ* high-pressure pair distribution function measurement and sound velocity measurement. The 29AS and 60AS glasses are regarded as Si-rich/Al-rich end-member compositions, and the 36AS, 43AS, and 50AS glasses consist of the two end-member phases at the nanoscale. The 29AS glass shows gradual changes in the intermediate-range order up to 9.3 GPa, similar to SiO_2 glass, while the 60AS glass exhibits a rapid structural change at 7.4–8.4 GPa, similar to $CaAl_2O_4$ glass. This rapid structural change causes a kink in the sound velocity–pressure trend near 8 GPa, as also observed in $CaAl_2O_4$ glass. In contrast, the Si-rich end-member 29AS glass does not exhibit the velocity kink. The Poisson's ratios of the five AS glasses and the SiO_2 glass start to converge above ~11 GPa, finally reaching a constant value of ~0.32 at a pressure of ~20 GPa. This result indicates that both the Si-rich and Al-rich end-members have a similar structure above ~20 GPa.

1. Introduction

Densely packed oxide (DPO) glasses synthesized by novel techniques such as the containerless levitation method have been attracting attention due to their enhanced functional properties, including high elastic modulus and hardness,[1,2] high crack resistance,[3] and high refractive index.[4,5] Such non-conventional glasses consist of various coordinated polyhedra (four-, five-, and six-fold units) that connect in various ways (corner-, edge-, and face-sharing) to yield high packing density.[6] This structure differs from that of conventional oxide glass, which has a three-dimensional random network of TO_4 tetrahedra (T: network former cation) connected by corner-sharing.

Al_2O_3–SiO_2 (AS) is one of the known systems from which DPO glasses can form. AS glass is a highly hard and tough[3] advanced functional material, and, in geoscience, it serves as an analogue for distinguishing the structural roles of Si and Al in magmas under pressure.[7,8] To discuss the relationship between structure and composition in this binary system, it is necessary to understand the structural differences between single-component glasses: SiO_2 and Al_2O_3 glasses. SiO_2 glass is the representative network glass, which has a three-dimensional Si–O network formed by the connection of corner-sharing SiO_4. The absence of network-modifier cations in SiO_2 glass results in a large cavity volume of ~30%,[9] which leads to low packing density. Conversely, Al^{3+} does not behave as a network former alone, and therefore, an Al_2O_3 melt cannot be vitrified by conventional melt–quenching techniques. Some recent techniques, such as the sol–gel method, thin-film fabrication, and anodization for metal Al, enable the vitrification of Al_2O_3. Al_2O_3 glass prepared by anodization contains ~60% Al ions in five- or six-coordination modes, and ~19% of the Al–O polyhedra exhibit edge-sharing connectivity.[10,11] Coexistence of the various structural units enables Al_2O_3 glass to achieve high packing density.

Binary AS glass is known to have a wide immiscibility gap, where the glasses are composed of nanoscale Si-rich and Al-rich domains.[12–16] For investigation of the local structure in each

---

[a] *Department of Chemistry, Gakushuin University, Tokyo 171-8588, Japan. E-mail: itaru.ohira@gakushuin.ac.jp*

[b] *Department of Physics and Astronomy, Kwansei Gakuin University, Sanda 669-1330, Japan*

[c] *Geodynamics Research Center, PIAS, Ehime University, Matsuyama 790-0826, Japan*

[d] *Institute for Planetary Materials, Okayama University, Misasa, Tottori 682-0193, Japan*

[e] *Japan Synchrotron Radiation Research Institute, Sayo-gun, Hyogo 679-5198, Japan*

[f] *High Pressure Collaborative Access Team, X-ray Science Division, Argonne National Laboratory, Argonne, Illinois 60439, USA*

[g] *Graduate School of Engineering, Kyoto University, Kyoto 615–8520, Japan*

domain, Liao *et al.* (2020) analysed 50 mol% Al_2O_3–50 mol% SiO_2 glass using electron energy loss fine structure spectroscopy conducted with a scanning transmission electron microscope.[14] Their analyses demonstrated that the Si-rich domain has a structure similar to that of SiO_2 glass, with corner-sharing $(Si,Al)O_4$ units that form a glass network. Conversely, ∼60% of the Al ions in the Al-rich domain exist in highly coordinated states (*i.e.*, AlO_5 and AlO_6), behaving as network modifiers, which is similar to Al_2O_3 glass. Although the range of immiscibility in this system has not been well constrained, the Al-rich end-member probably has a mullite-like composition (approximately 60 mol% Al_2O_3–40 mol% SiO_2, 60AS).[15,16] In addition, an NMR study on the 60AS glass showed that it contains Al in 4-, 5-, and 6-fold coordination states in an approximate ratio of 4 : 5 : 1.[17] The presence of highly coordinated Al is consistent with the pioneering XRD, Raman, and NMR measurements conducted on 60AS glass synthesized using other novel techniques.[18–22] Therefore, the Al-rich domain formed in the immiscible region is considered to be a densely packed structure similar to Al_2O_3 glass.

In addition to the compositional effect, pressure is another important factor in the formation of densified glasses. Under room temperature compression, SiO_2 glass exhibits an almost linear increase in density up to at least 20 GPa.[23–25] The density change may result from multiple densification processes. It has been reported that SiO_2 glass experiences collapse of the silicon's second shell into the first shell, which breaks local tetrahedral symmetry, at the pressure region above 2.3 GPa.[26] After completion of this breaking of the local tetrahedral symmetry, its nearest-neighbour Si–O coordination number (CN) changes from 4 to 6 at ∼10–40 GPa.[27–32] These two different structural changes result in distinct behaviours of sound velocity. The breaking of local tetrahedral symmetry yields an anomalous elasticity minimum under compression around that pressure region,[33–36] while the Si–O CN increase above 10 GPa causes a gradual increase in longitudinal wave velocity (v_L) and the transverse wave velocity (v_T).[34–36] Such pressure-induced densification is also thought to occur in DPO glass. However, the structural changes may differ from those of the network glass with large void volumes. For example, a study on $CaAl_2O_4$ glass, which is a DPO glass, showed a pressure-induced polyamorphic transition accompanied by a discontinuous increase in v_L and v_T over the narrow pressure range of 8–10 GPa, driven by the disappearance of the large voids between the Ca and O atoms.[36] Similar to the $CaAl_2O_4$ glass, the highly coordinated Al ions in the Al-rich end-member in the AS glass may play a role similar to that of the Ca ions in that aluminate glass.

In this study, we have investigated the pressure-induced changes in structure and elastic properties of xAl_2O_3–$(100 - x)SiO_2$ glasses (x = 29, 36, 43, 50, 60 mol%; referred to as xAS). The AS glasses were prepared across the immiscible region of the Al_2O_3–SiO_2 system. The 29AS and 60AS homogeneous glasses are defined as the Si-rich and Al-rich end-members, respectively, while the 36AS, 43AS, and 50AS glasses exhibit nano-scale phase separation and are composed of the two end-members. To understand the high-pressure structural changes in the Si-rich and Al-rich end-members, the structure factor $S(Q)$ and the pair-distribution function $g(r)$ were determined for the 29AS and 60AS glasses. In addition, the sound velocity and Poisson's ratio of the five AS glasses under pressure were determined. Based on the structural data and velocity–pressure trends of the AS glasses, we conclude that the Al-rich end-member undergoes a rapid structural change characterized by a velocity kink near 8 GPa, followed by structural convergence with the Si-rich end-member above ∼20 GPa.

2. Experimental methods

2.1. Sample synthesis and chemical analysis

Five xAl_2O_3–$(100 - x)SiO_2$ glasses (x = 29, 36, 43, 50, and 60, referred to as 29AS, 36AS, 43AS, 50AS, and 60AS) were synthesized using a containerless laser-heating levitation method. We used the 50AS and 60AS glasses reported in ref. 3. In addition, we synthesized three samples (29AS, 36AS, and 43AS glasses) using an aerodynamic levitator with a 200 W CO_2 laser at GRC, Ehime University. For the synthesis of the three glasses, SiO_2 (quartz, 99.9%, *ca.* 4 μm, Kojundo Chemical Laboratory) and Al_2O_3 (>99%, Wako) powders were heated at 1473 K for 2 h in air by an electric furnace to remove water. The dried powders were weighed with the stoichiometric ratios of xAl_2O_3–$(100 - x)SiO_2$ (x = 20, 30, 40) and were mixed in ethanol using an agate mortar for 1 h. The powder mixtures were compressed to a cylindrical shape by a pellet die (2 mm in diameter), which were melted in the aerodynamic levitation furnace by laser heating. After confirmation of total melting by a high-speed camera, we turned off the laser for quenching the spherical melt sample to form glass. Because of the evaporation of SiO_2 during melt processing, the Al_2O_3 contents in the synthesized glasses are higher than those in the starting powders.[12] Indeed, the compositions of the 29AS (Al_2O_3 = 28.59 ± 0.14 mol%, n = 20), 36AS (36.11 ± 0.07, n = 20), and 43AS (42.92 ± 0.07, n = 30) glasses—prepared from the starting powder compositions with x = 20, 30, 40—were determined by scanning electron microscopy (JEOL JMS-6360) with energy-dispersive spectroscopy (Oxford INCA energy 300) at Gakushuin University.

The analyses of the AS glass samples recovered after the high-pressure ultrasonic measurements were performed using a JEOL JEM 2100F field emission scanning transmission electron microscope (STEM) operating system equipped with a JEOL JED-2300T energy dispersive X-ray spectrometer (EDS). The EDS data were obtained and processed using a Thermo Fischer Scientific Noran System 7. A thin foil of about 100 nm thick was prepared using a focused ion beam (FIB) lift-out technique using a Thermo Fisher Scientific Scios and Scios2 dual-beam FIB-SEM system.

2.2. *In situ* high-pressure pair distribution function measurements

The structure factors, $S(Q)$, of the 60AS glass under pressure were obtained by *in situ* multiangle energy-dispersive X-ray diffraction (EDXD) measurements in a Paris-Edinburgh press at the beamline 16-BM-B of the APS. Details of the high-pressure experimental setup at beamline 16-BM-B and the analytical procedures have been reported previously.[36,37] We used a cupped-Drickamer-toroidal (CDT) cell, the same as that used in a previous study on $CaAl_2O_4$ glass.[36] A piece of gold was placed at the edge of the glass sample to avoid contamination of its X-ray diffraction peaks into that of the glass sample. The gold was used for the determination of experimental pressure by the equation of state of gold.[38] In the high-pressure multi-angle EDXD measurements, we collected a series of EDXD patterns of the 60AS glass sample at 2θ angles of 3.0, 4.0, 5.0, 7.0, 9.0, 12.0, 15.0, 18.0, 22.0, 26.0, 30.0, and 35.0° at each pressure point. The $S(Q)$ was determined from the collected EDXD patterns using the software packages hpMCA and aEDXD developed in the 16-BM-B beamline.[37,39] The pair distribution function $g(r)$ was calculated from the Fourier transform of the $S(Q)$. The sample density (ρ) at high pressure (P) used in this Fourier transform is estimated from the results of the high-pressure sound velocity measurement using the ambient density (ρ_0) through the relationship:

$$\rho = \rho_0 + \int_{P_0}^{P} \frac{\gamma}{\left(v_L{}^2 - \frac{4}{3}v_T{}^2\right)} \mathrm{d}P, \qquad (1)$$

where P_0 is the initial pressure (10^{-4} GPa), v_L and v_T are the longitudinal and transverse wave velocities, and γ is the ratio of the isothermal and adiabatic bulk moduli that is taken to be 1 for the samples at room temperature.

The $S(Q)$ values of the 29AS glass were obtained by *in situ* angle-dispersive X-ray diffraction (ADXD) measurements at the BL15XU beamline in SPring-8. We used a pink beam at a photon energy of 100.34 keV. Similar to the EDXD measurements, we used a CDT cell in the Paris-Edinburgh press for the high-pressure experiments, and gold was used as the pressure scale.[38] XRD patterns were collected at 2θ angles between 0.4 and 16.8°. The details of the experimental setup and analytical process of $S(Q)$ and $g(r)$ were reported elsewhere.[40] The density of the 29AS glass was estimated from its sound velocity data, similar to that of the 60AS glass.

2.3. *In situ* high-pressure sound velocity measurement

The sound velocities of the five AS glasses at high pressures were determined by *in situ* X-ray and ultrasonic measurements in a Kawai-type 1500 ton multi-anvil press (SPEED-1500) at the beamline BL04B1 in SPring-8.[41,42] The cell assembly used in the study is shown in Fig. S1. The glass samples were shaped into a cylindrical shape (1.5 or 2.0 mm in diameter and ~1 mm in length) and placed at the centre of a MgO sleeve. Both sides of the samples were polished using a 0.5 μm diamond polishing mat. We placed an Al_2O_3 buffer rod for transmitting elastic waves from the WC anvil to the sample, and a backing material (NaCl with 10 wt% gold) was placed at the back side of the sample. Gold foil (2 μm thickness) was inserted between each interface (buffer rod/sample and sample/backing material) to enhance mechanical coupling for elastic wave propagation and to mark sample interfaces for sample length measurement.

White X-ray radiography images were obtained using a CMOS camera with a resolution of 1.31 μm per pixel. The sample length was determined from the distance between the two gold foils on the top and bottom faces of the sample at each pressure point.[41,43] For pressure determination, energy-dispersive X-ray diffraction (EDXD) measurements were conducted for the backing material (mixture of NaCl and Au) at a fixed diffraction angle of 5.9980° (29AS), 5.9988° (36AS), 5.9778° (43AS), 6.0071° (50AS), or 6.0069° (60AS). The gold in the backing material was used as a pressure scale.[38] Ultrasonic measurements were carried out at each pressure condition using the pulse–echo-overlap method. The acoustic echo measurements were performed at a frequency of 50–70 MHz for the longitudinal waves and 30–50 MHz for the transverse waves. The two-way travel time was analysed using an analysis program,[43] and the mean and standard deviation of the travel times obtained from different frequencies are defined as the best estimate and error, respectively. The errors of travel time were up to 0.6% (longitudinal wave) and 0.4% (transverse wave), respectively. The errors of the sample length analysis were up to ±6.7 pixels (± 9 μm, 1.2%). The overall uncertainties of the longitudinal and transverse wave velocities (v_L and v_T, respectively) were up to 1.2%. The numerical data of v_L and v_T with their uncertainties are shown in Tables S1–S5 in the SI.

3. Results and discussion

3.1. Nano-texture in the AS glasses

Fig. 1 exhibits the annular dark-field (ADF)-STEM images of the AS glasses recovered after the high-pressure sound velocity measurements. The 60AS glass has a homogenous texture (Fig. 1a), while the 50AS (Fig. 1b), 43AS (Fig. 1c), and 36AS (Fig. 1d) glasses show nano-scale phase separation. The 50AS, 43AS, and 36AS glasses are composed of nano-scale Si-rich and

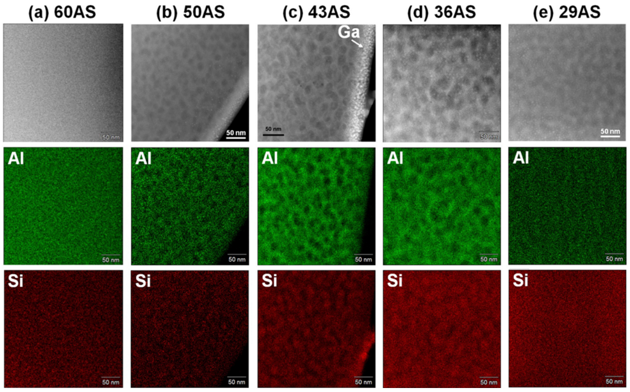

Fig. 1 ADF-STEM images of the (a) 60AS, (b) 50AS, (c) 43AS, (d) 36AS, and (e) 29AS glasses recovered from *in situ* high-pressure X-ray ultrasonic measurements. The top, middle, and bottom rows exhibit the ADF-STEM images and the elemental mapping images for Al and Si in each sample, respectively. The white particles on the ADF-STEM images are gallium (Ga) deposition contamination formed during FIB processing.

Al-rich domains (Fig. 1b–d and Table S6). The 50AS glass exhibits binodal decomposition, in which the Si-rich domains of ∼10–20 nm in size are isolated (Fig. 1b), as observed in the previous STEM analysis.[14] In contrast, the 43AS glass has a morphology of spinodal decomposition, where the nano-scale Si-rich domains were interconnected in a similar way to the Al-rich matrix (Fig. 1c). Compared to the 43AS glass, the connections between the Si-rich domains become more developed in the 36AS glass (Fig. 1d). The transition boundary from the spinodal regime to the binodal regime lies between 50AS and 43AS, which is consistent with previous thermodynamic analysis.[15] The 29AS glass appears to show two textures in the ADF-STEM image (Fig. 1e). However, the STEM-EDS analyses show no compositional difference between the dark and bright domains (Table S6). These results indicate that the 36AS, 43AS, and 50AS glasses have a nano-scale phase separation texture, while the 60AS and 29AS glasses can be regarded as homogeneous glasses composed of Al-rich and Si-rich end-members within the investigated composition range, respectively.

3.2. Structure factor $S(Q)$ and pair-distribution function $g(r)$ of AS glasses under compression

Fig. 2 exhibits the experimentally determined $S(Q)$ and $g(r)$ of the 29AS (Si-rich end-member) and 60AS (Al-rich end-member) glasses at high-pressure conditions from 0.4 GPa to 9.5 GPa. In the 29AS glass, the intensity of the first sharp diffraction peak (FSDP) decreases together with the shift of the peak position to high-Q up to 9.3 GPa (Fig. 2a). The behaviour of the FSDP in the 29AS glass is similar to that of SiO_2 glass.[26,28,32] The FSDP in the $S(Q)$ of the 60AS glass also shifts to higher Q, but it does not show a clear intensity reduction up to 7.4 GPa (Fig. 2b). Above 7.4 GPa, however, the intensity begins to increase, which is similar to the observation in $CaAl_2O_4$ glass.[36]

In addition to the changes in the FSDPs, the second peaks at ∼3 $Å^{-1}$ grow with increasing pressure. The second peak of the 29AS glass gradually grows over the experimental pressure range (Fig. 2a). The development of the second peaks is likely attributed to the breaking of local tetrahedral symmetry and an increase in packing density of oxygen atoms, as reported in the pressurised SiO_2 glass.[26,30,44] Conversely, the second peak of the 60AS exhibits no clear change in its intensity below 7.4 GPa, and it abruptly increases between 7.4–8.4 GPa (Fig. 2b). Unlike SiO_2 glass, the 60AS glass does not have the tetrahedral symmetry due to the presence of the 5- and 6-fold Al ions. The abrupt intensity increase observed in the 60AS glass can be attributed to an increase in topological ordering due to a transition to a more densely packed structure, as observed in $CaAl_2O_4$ glass.[36]

Fig. 2c and d show the $g(r)$ of the 29AS and 60AS glasses, derived from the experimentally determined $S(Q)$ (Fig. 2a and b). The first peak ($r1$) in the $g(r)$ is assigned to the average T–O bond distance (T = Al, Si). As the ionic radii of the 4-, 5-, and 6-fold coordinated Al^{3+} (0.39, 0.48, 0.535 Å) are larger than that of the 4-fold Si^{4+} (0.26 Å),[45] the $r1$ shifts to higher r with increasing Al_2O_3 content. The $r1$ of the 29AS glass stays at ∼1.64 Å up to 9.4 GPa (Fig. S3). This behaviour is similar to that of the SiO_2 glass, where the Si–O bond distance and CN start to increase above ∼10–15 GPa.[27–29] Conversely, the $r1$ of the 60AS glass is located at ∼1.75 Å below 7.4 GPa, and starts to shift toward the high-r side at high pressures (Fig. S4). The result

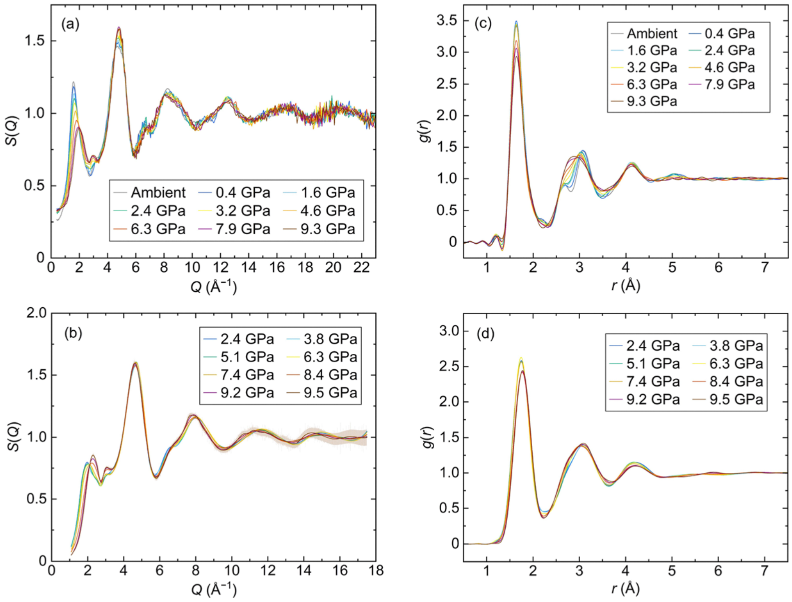

Fig. 2 Total structure factor $S(Q)$ and pair-distribution functions $g(r)$ for the 29AS and 60 AS glasses at high-pressure conditions. (a) The $S(Q)$ of the 29 AS glass obtained by the ADXD measurement at the BL15XU, SPring-8. (b) The $S(Q)$ of the 60 AS glass obtained by *in situ* multiangle EDXD measurement at the 16-BM-B, APS. (c) The $g(r)$ of the 29AS glass determined from the $S(Q)$ shown in (a). (d) The $g(r)$ of the 60AS glass determined from the $S(Q)$ shown in (b). The typical size of the error in the EDXD measurements is indicated by the brown vertical bars for the $S(Q)$ data at 9.5 GPa. The $S(Q)$ and $g(r)$ data with offsets to avoid overlap of each pattern are provided in Figs. S2 and S3 in the SI.

indicates that the average T–O CN of the 60AS glass starts to increase from ∼8 GPa. It has been reported that the T–O CN of the 60AS glass reaches six at ∼20 GPa, with a T–O bond length of ∼1.81 Å.[8]

The difference in $g(r)$ between the two glasses becomes more obvious in the long correlations. The unpressurised 29AS glass is considered to be dominated by a network formed by corner-sharing TO_4 tetrahedra, resulting in the development of two peaks due to the correlations of O–O at ∼2.6 Å (the second peak) and corner-sharing T–T (the third peak) at ∼3.0 Å (Fig. 2c), same as SiO_2 glass (*e.g.*, ref. 27). As the pressure increases, the second and third peaks gradually converge, eventually merging into a single peak (Fig. 2c). This is explained by the decrease in the T–T distance, likely due to bending of the T–O–T inter-tetrahedral angles upon compression, similar to the observation in SiO_2 glass,[27,32] which supports the structural analogy between 29AS and SiO_2 glass. In contrast, the unpressurised 60AS glass contains various correlations due to O–O bonds, corner- and edge-sharing T–T interactions, and the second nearest-neighbour T–O in the r range between ∼2.6 Å and ∼3.4 Å, even at ambient pressure.[19,20] This results in a broad peak without clear pressure dependence (Fig. 2d). This static behaviour of the merged peak around 3 Å is similar to that of $CaAl_2O_4$ glass, which is one of the DPO glasses.[36] Interestingly, the 29AS and 60AS glasses show similar $g(r)$ at the highest pressure. This result implies that both the 29AS and 60AS glasses have a similar intermediate-range framework above ∼10 GPa.

3.3. Sound velocity–pressure trends of the AS glasses up to 24 GPa and their structural significance

Fig. 3 exhibits the v_L and v_T of the five AS glasses under compression to 24.3 GPa, determined by *in situ* high-pressure ultrasonic measurements at the BL04B1 beamline, SPring-8. The velocity–pressure trends of the SiO_2 glass determined from the previous ultrasonic measurements are also shown.[33,36] The SiO_2 glass shows a rapid decrease in v_L and v_T up to ∼2–3 GPa, followed by a linear increase up to at least ∼20 GPa. The 29AS glass (Si-rich end-member) exhibits v_L–P and v_T–P trends, as well as changes in $S(Q)$ and $g(r)$, similar to SiO_2 glass (Fig. 2). However, the pressure at which the velocity minimum is found increases to a higher pressure of ∼5 GPa (5.1 GPa for v_L and 4.6 GPa for v_T) (Fig. 3 and Table S1). In addition, the v_L and v_T values of the 29AS glass are higher than those of SiO_2 glass. This indicates that the 29AS glass is stiffer than SiO_2 glass because the bulk and shear moduli increase with increasing Al_2O_3 content in the binary aluminosilicate glasses.[3]

On the other hand, the v_L–P and v_T–P trends of the 60AS glass (Al-rich end-member) are similar to those of $CaAl_2O_4$ glass up to 24 GPa (Fig. 3). The velocity minima are observed at 7.7 GPa for both v_L and v_T, and then the velocities rapidly increase up to 11.3 GPa, followed by a linear increase at higher pressure (Fig. 3 and Table S5). As a result, the 60AS glass shows kinks in the dv_L/dP and dv_T/dP slopes (hereafter, "velocity kink") in the 8–11 GPa pressure region. In addition to the velocity kink, this glass also exhibits a rapid reduction of sample length in this pressure region (Fig. S5). These elastic anomalies in this pressure region are also observed in $CaAl_2O_4$ glass.[36] Above ∼11 GPa, however, both the two end-member glasses exhibit a linear increase in velocity with almost the same slope (29AS: $dv_L/dP = 0.1279(13)$, $dv_T/dP = 0.0496(9)$; 60AS: $dv_L/dP = 0.0987(20)$, $dv_T/dP = 0.0416(9)$; Table S7). The gradual velocity increase in the 29AS and 60AS above ∼11 GPa likely reflects the gradual increase in average T–O CN, which is also observed in SiO_2[34–36] and $CaAl_2O_4$[36] glasses.

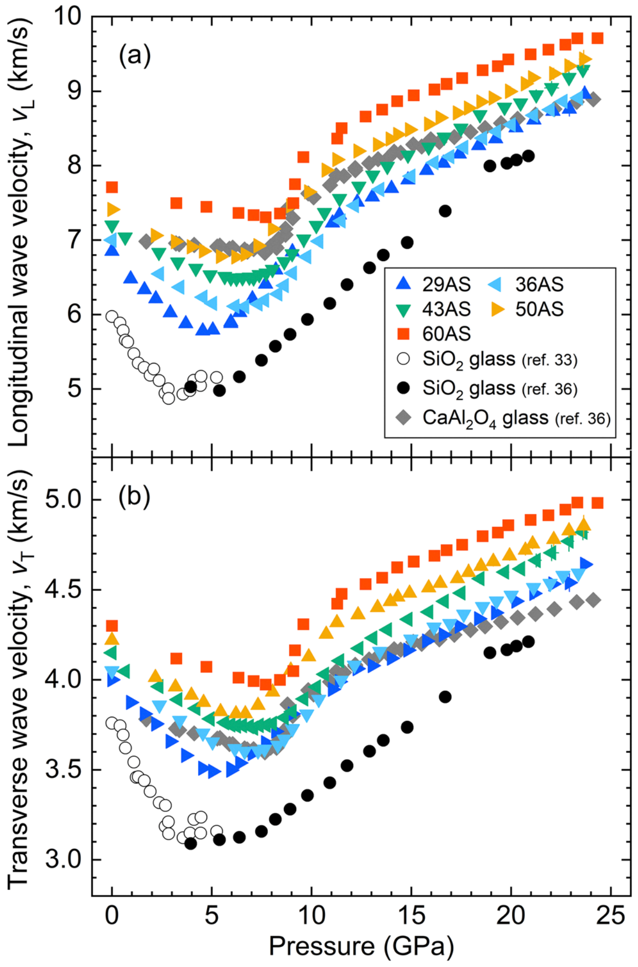

Fig. 3 (a) Longitudinal wave velocity (v_L) and (b) transverse wave velocity (v_T) of the five AS glasses (this study), SiO_2 glass,[33,36] and $CaAl_2O_4$ glass[36] determined by the ultrasonic method under compression. The sound velocities at atmospheric pressure (10^{-4} GPa) are estimated from the previously measured data.[3] The numerical data of the AS glasses are shown in Tables S1–S5 in the SI.

The onset of the velocity kink for the 60AS glass is observed at a pressure where the FSDP and second peak in $S(Q)$ increase in intensity (Fig. 2a), and the $r1$ in $g(r)$ starts to shift to high r (Fig. 2c and Fig. S4). Therefore, the 60AS glass, which has a densely packed structure even at ambient conditions, transforms into a more densely packed state at ∼8 GPa. Interestingly, the NMR spectroscopic studies of the Al_2O_3 and $Mg_3Al_2Si_3O_{12}$ glasses cycled to high pressure demonstrated that the irreversible increase of the Al–O CN progresses only in the

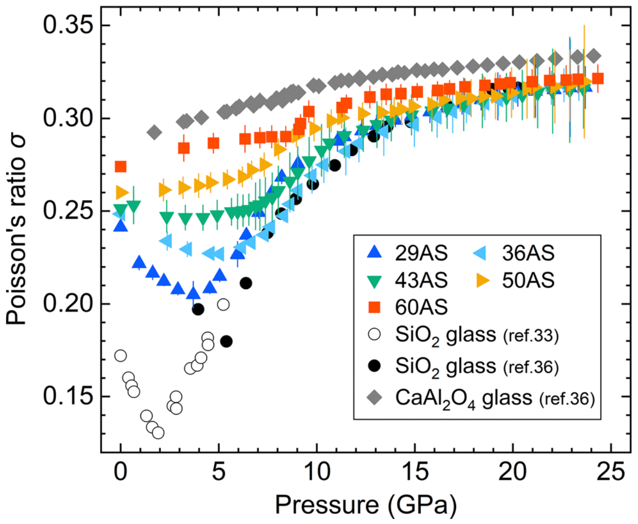

Fig. 4 Poisson's ratio (σ) of the five AS glasses (this study), SiO_2 glass,[33,36] and $CaAl_2O_4$[36] calculated from the sound velocity data. The numerical data of the AS glasses are shown in Tables S1–S5 in the SI.

~6–10 GPa region, and that the fraction of high-coordinated Al^{3+} ions preserved in the decompressed samples does not change above ~12 GPa.[46,47] Therefore, the structural changes accompanied by the velocity kink around 8 GPa may cause the irreversible densification. Indeed, it has been confirmed that $CaAl_2O_4$ glass recovered following exposure to 16 GPa (~6 GPa higher than the end point of velocity kink) undergoes irreversible densification.[36]

The velocity–pressure trends of the 36AS, 43AS, and 50AS glasses, which have nano-scale phase separation textures, exhibit a velocity kink and reduction of sample length at ~7–11 GPa (Fig. 3 and S5). Based on the presence of the elastic anomalies, the pressure-induced structural changes that occurred in the three glasses are more similar to the 60AS glass than to the 29AS glass. Moreover, the velocity kink becomes unclear with decreasing Al_2O_3 content (corresponding to an increase in the Si-rich domain) (Fig. 3). As the three phase-separating glasses contain Al-rich domains (Fig. 1b–d and Table S6) that can behave similarly to the 60AS glass, their velocity kinks are considered to be caused by rapid structural changes in these domains.

3.4. Structural convergence of the AS glasses above 20 GPa

Poisson's ratio (σ) is calculated using the measured v_L and v_T by the following equation:

$$\sigma = \frac{{v_L}^2 - 2{v_T}^2}{2({v_L}^2 - {v_T}^2)}. \tag{2}$$

Poisson's ratio is known to increase with increasing atomic packing density (C_g), and the C_g correlates with the glass network dimensionality (*e.g.*, ref. 48). For example, SiO_2 and Si-rich silicate glasses that have a three-dimensional random network with a large fraction of free volume exhibit small Poisson's ratios (σ < 0.2). On the other hand, the DPO glasses, such as Al-rich aluminosilicate and aluminate glasses containing various structural motifs (network modifier 5- and 6-fold Al^{3+}, edge-sharing AlO_x polyhedra), lose their fully polymerized three-dimensional networks even at ambient conditions, which leads to their high Poisson's ratios and C_g.[48] Consequently, in the Al_2O_3–SiO_2 system, the Poisson's ratio of the unpressurised glasses ranges from 0.190 for the SiO_2 glass to 0.274 for the 60AS glass.[3] This reflects the progression of the densely packed state due to the addition of Al_2O_3. In the initial stage of pressurisation below ~5 GPa, the Poisson's ratio of the 29AS, 36AS, and 43AS glasses exhibits negative pressure dependence, while those of the 50AS and 60AS glasses exhibit positive pressure dependence (Fig. 4). Above 5 GPa, all of the AS glasses show positive pressure dependence (Fig. 4). At ~5–8 GPa, the increased rate of σ change increases with Al_2O_3 content, resulting in the σ of the 29AS glass being larger than those of the 36AS and 43AS glasses.

After the completion of the velocity kink at ~11 GPa, the difference in the σ values among the AS glasses becomes small, and they finally converge to ~0.32 at ~20 GPa (Fig. 4). This result implies that both of the Si-rich and Al-rich end-members of our study have a very similar atomic packing state at that pressure. The converged value of 0.32 is comparable with those of metallic glasses (σ = 0.3–0.4).[49,50] Metallic glasses have a zero-dimensional cluster-based network.[48] Therefore, both the Si-rich and Al-rich end-member glasses are considered to have such a weakly correlated network at >20 GPa.

Conclusions

We conducted *in situ* high-pressure pair-distribution function and sound velocity measurements on AS glass samples. The 29AS glass, a Si-rich end-member glass within the investigated composition range, exhibits a gradual change in the intermediate-range order up to 9.3 GPa, similar to that observed in SiO_2 glass. In contrast, the 60AS glass, an Al-rich end-member glass, shows changes in both the intermediate- and short-range orders only at 7.4–8.4 GPa. The sound velocity data indicate that the densification process of the AS glasses is divided into three distinct pressure regions: (i) the low-pressure region up to the velocity minimum; (ii) the middle-pressure region, where v_L and v_T quickly increase (the velocity kink); and (iii) the high-pressure region with a gentle and linear gradient. In region (i), the variation in the velocity–pressure trends of the AS glasses likely arise from the differences in the C_g values of the initial structures. In region (ii), the velocity kink becomes distinct with increasing Al_2O_3 content, indicating that the Al-rich end-member undergoes a rapid structural change at ~7–11 GPa, resulting in the velocity kink. In region (iii), the Poisson' ratios of the five AS glasses and SiO_2 glass converge, and finally become the same within error. This result indicates that at >20 GPa, both the Si-rich and Al-rich end-member phases are considered to have a weakly correlated network, such as the zero-dimensional cluster-based network observed in metallic glasses.

Author contributions

I. Ohira: conceptualization, data curation, formal analysis, funding acquisition, investigation, methodology, project administration, resources, visualization, and writing – original draft. Y. Kono: funding acquisition, investigation, software, and writing – review and editing. S. Gréaux: formal analysis, funding acquisition, investigation, methodology, and resources. S. Inoué: investigation, visualization, writing-review and editing. N. M. Kondo: investigation. S. Kakizawa: investigation, resources, and software. Y. Higo: resources and software. N. Tsujino: resources and software. R. Hrubiak: resources, software, and writing – review and editing. G. Shen: investigation and resources. A. Masuno: resources.

Conflicts of interest

There are no conflicts to declare.

Data availability

The authors confirm that the data supporting the findings of this study are available within the article and its supplementary information (SI). Supplementary information: schematic diagram of the high-pressure cell for sound velocity measurement, the $S(Q)$ and $g(r)$ data with vertical offset, pressure dependences of the $r1$ and the sample length, and numerical values of the measured sound velocity and chemical composition. See DOI: https://doi.org/10.1039/d6ma00275g.

Acknowledgements

This paper is supported by JSPS KAKENHI (grants no. JP20K22369, JP23K13193, JP22K18736, JP23KK0065, JP19H02002, and JP23K25970) and the Joint Usage/Research Center PRIUS, Ehime University, Japan. The experiments were conducted at the BL04B1 and BL15XU beamlines at SPring-8 (JASRI proposal No. 2020A0069, 2020A1712, and 2022B1171). A part of this research was performed using an APS beam time award (DOI: https://doi.org/10.46936/APS-178398/60015783) from the Advanced Photon Source, a U.S. Department of Energy (DOE) Office of Science user facility operated for the DOE Office of Science by Argonne National Laboratory under contract no. DE-AC02-06CH11357. HPCAT operations are supported by DOE-NNSA's Office of Experimental Sciences.

References

1 G. A. Rosales-Sosa, A. Masuno, Y. Higo, H. Inoue, Y. Yanaba, T. Mizoguchi, T. Umada, K. Okamura, K. Kato and Y. Watanabe, *Sci. Rep.*, 2015, **5**, 15233.
2 Y. Guo, J. Li, Y. Zhang, S. Feng and H. Sun, *iScience*, 2021, **24**, 102735.
3 G. A. Rosales-Sosa, A. Masuno, Y. Higo and H. Inoue, *Sci. Rep.*, 2016, **6**, 23620.
4 Y. Arai, K. Itoh, S. Kohara and J. Yu, *J. Appl. Phys.*, 2008, **103**, 094905.
5 A. Masuno and H. Inoue, *Appl. Phys. Express*, 2010, **3**, 102601.
6 A. Masuno, *J. Phys. Soc. Jpn.*, 2022, **91**, 091003.
7 I. Ohira, M. Murakami, S. Kohara, K. Ohara and E. Ohtani, *Prog. Earth Planet. Sci.*, 2016, **3**, 18.
8 I. Ohira, Y. Kono, C. Kenney-Benson, A. Masuno and G. Shen, *Geochem. Persp. Lett.*, 2019, **10**, 41–45.
9 S. Kohara, J. Akola, H. Morita, K. Suzuya, J. K. R. Weber, M. C. Wilding and C. J. Benmore, *Proc. Natl. Acad. Sci. U. S. A.*, 2011, **108**, 14780–14785.
10 H. Hashimoto, K. Yazawa, H. Asoh and S. Ono, *J. Phys. Chem. C*, 2017, **121**, 12300–12307.
11 H. Hashimoto, Y. Onodera, S. Tahara, S. Kohara, K. Yazawa, H. Segawa, M. Murakami and K. Ohara, *Sci. Rep.*, 2022, **12**, 516.
12 S. K. Wilke, C. J. Benmore, V. Menon, J. Ilavsky, A. Rezikyan, R. E. Youngman, M. P. Carson and R. Weber, *J. Am. Ceram. Soc.*, 2023, **106**, 2820–2834.
13 S. Sen and R. E. Youngman, *J. Phys. Chem. B*, 2004, **108**, 7557–7564.
14 K. Liao, A. Masuno, A. Taguchi, H. Moriwake, H. Inoue and T. Mizoguchi, *J. Phys. Chem. Lett.*, 2010, **11**, 9637–9642.
15 S. H. Risbud and J. A. Pask, *J. Am. Ceram. Soc.*, 1977, **60**, 418–424.
16 M. Djuric and A. Mihajlov, *J. Am. Ceram. Soc.*, 1996, **79**, 1252–1256.
17 R. Weber, S. Sen, R. E. Youngman, R. T. Hart and C. J. Benmore, *J. Phys. Chem. B*, 2008, **112**, 16726–16733.
18 P. McMillan and B. Piriou, *J. Non-Cryst. Solids*, 1982, **53**, 279–298.
19 H. Morikawa, S. Miwa, M. Miyake, F. Marumo and T. Sata, *J. Am. Ceram. Soc.*, 1982, **65**, 78–81.
20 M. Okuno, N. Zotov, M. Schmücker and H. Schneider, *J. Non-Cryst. Solids*, 2005, **351**, 1032–1038.
21 R. K. Sato, P. F. McMillan, P. Dennison and R. Dupree, *J. Phys. Chem.*, 1991, **95**, 4483–4489.
22 B. T. Poe, P. F. McMillan, C. A. Angell and R. K. Sato, *Chem. Geol.*, 1992, **96**, 333–349.
23 C. Meade and R. Jeanloz, *Phys. Rev. B:Condens. Matter Mater. Phys.*, 1987, **35**, 236–244.
24 T. Sato and N. Funamori, *Phys. Rev. B:Condens. Matter Mater. Phys.*, 2008, **101**, 255502.
25 S. Petitgirard, W. J. Malfait, B. Journaux, I. E. Collings, E. S. Jennings, I. Blanchard, I. Kantor, A. Kurnosov, M. Cotte, T. Dane, M. Burghammer and D. C. Rubie, *Phys. Rev. Lett.*, 2017, **119**, 215701.
26 Y. Kono, K. Ohara, N. M. Kondo, H. Yamada, S. Hiroi, F. Noritake, K. Nitta, O. Sekizawa, Y. Higo, Y. Tange, H. Yumoto, T. Koyama, H. Yamazaki, Y. Senba, H. Ohashi, S. Goto, I. Inoue, Y. Hayashi, K. Tamasaku, T. Osaka, J. Yamada and M. Yabashi, *Nat. Commun.*, 2022, **13**, 2292.
27 C. Meade, R. J. Hemley and H. K. Mao, *Phys. Rev. Lett.*, 1992, **69**, 1387–1390.
28 C. J. Benmore, E. Soignard, S. A. Amin, M. Guthrie, S. D. Shastri, P. L. Lee and J. L. Yarger, *Phys. Rev. B:Condens. Matter Mater. Phys.*, 2010, **81**, 054105.

29 T. Sato and N. Funamori, *Phys. Rev. B:Condens. Matter Mater. Phys.*, 2010, **82**, 184102.

30 A. Zeidler, K. Wezka, R. F. Rowlands, D. A. J. Whittaker, P. S. Salmon, A. Polidori, J. W. E. Drewitt, S. Klotz, H. E. Fischer, M. C. Wilding, C. L. Bull, M. G. Tucker and M. Wilson, *Phys. Rev. Lett.*, 2014, **113**, 135501.

31 C. Prescher, V. B. Prakapenka, J. Stefanski, S. Jahn, L. B. Skinner and Y. Wang, *Proc. Natl. Acad. Sci. U. S. A.*, 2017, **114**, 10041–10046.

32 Y. Kono, Y. Shu, C. Kenney-Benson, Y. Wang and G. Shen, *Phys. Rev. Lett.*, 2020, **125**, 205701.

33 A. Yokoyama, M. Matsui, Y. Higo, Y. Kono, T. Irifune and K.-I. Funakoshi, *J. Appl. Phys.*, 2022, **107**, 123530.

34 C.-S. Zha, R. J. Hemley, H.-k Mao, T. S. Duffy and C. Meade, *Phys. Rev. B:Condens. Matter Mater. Phys.*, 1994, **50**, 13105–13112.

35 C. Weigel, M. Mebarki, S. Clément, R. Vacher, M. Foret and B. Rufflé, *Phys. Rev. B*, 2019, **100**, 094102.

36 I. Ohira, Y. Kono, S. Gréaux, J. W. E. Drewitt, S. Jahn, F. Noritake, K. Ohara, S. Hiroi, N. M. Kondo, R. Hrubiak, Y. Higo, N. Tsujino, S. Kakizawa, K. Nitta and O. Sekizawa, *Phys. Rev. B*, 2024, **110**, 054115.

37 Y. Kono, C. Park, C. Kenney-Benson, G. Shen and Y. Wang, *Phys. Earth Planet. Inter.*, 2014, **228**, 269–280.

38 T. Tsuchiya, *J. Geophys. Res.: Solid Earth*, 2003, **108**, 2462.

39 R. Hrubiak and M. L. Rivers, *High Press. Res.*, 2023, **43**, 175–191.

40 Y. Kono, K. Ohara, N. M. Kondo, Y. Higo, S. Kakizawa, H. Yumoto, T. Koyama, H. Yamazaki, Y. Senba, H. Ohashi, I. Inoue, Y. Hayashi and M. Yabashi, *Rev. Sci. Instrum.*, 2024, **95**, 013904.

41 Y. Higo, Y. Kono, T. Inoue, T. Irifune and K.-I. Funakoshi, *J. Synchrotron. Rad.*, 2009, **16**, 762–768.

42 Y. Higo, T. Irifune and K.-I. Funakoshi, *Rev. Sci. Instrum.*, 2018, **89**, 014501.

43 Y. Kono, C. Park, T. Sakamaki, C. Kenney-Benson, G. Shen and Y. Wang, *Rev. Sci. Instrum.*, 2012, **83**, 033905.

44 Y. Onodera, S. Kohara, P. S. Salmon, A. Hirata, N. Nishiyama, S. Kitani, A. Zeidler, M. Shiga, A. Masuno, H. Inoue, S. Tahara, A. Polidori, H. E. Fischer, T. Mori, S. Kojima, H. Kawaji, A. I. Kolesnikov, M. B. Stone, M. G. Tucker, M. T. McDonnell, A. C. Hannon, Y. Hiraoka, I. Obayashi, T. Nakamura, J. Akola, Y. Fujii, K. Ohara, T. Taniguchi and O. Sakata, *NPG Asia Mater.*, 2020, **12**, 85.

45 R. D. Shannon, *Acta Crystallogr., Sect. A*, 1976, **32**, 751–767.

46 S. K. Lee, K. Y. Mun, Y.-H. Kim, J. Lhee, T. Okuchi and J.-F. Lin, *J. Phys. Chem. Lett.*, 2020, **11**, 2917–2924.

47 S. K. Lee, E. El Ghazaoui, J. J. Kweon, S. Lee and J.-H. Parq, *Nat. Commun.*, 2025, **16**, 9930.

48 T. Rouxel, *J. Am. Ceram. Soc.*, 2007, **90**, 3019–3039.

49 W. H. Wang, C. Dong and C. H. Shek, *Mater. Sci. Eng.*, 2004, **R44**, 45–89.

50 W. H. Wang, *Prog. Mater. Sci.*, 2012, **57**, 487–656.